DOI: 10.1002/asia.201000032

Lanthanide (Eu^{3+}, Tb^{3+}) Centered Mesoporous Hybrids with 1,3-Diphenyl-1,3-Propanepione Covalently Linking SBA-15 (SBA-16) and Poly(methylacrylic acid)

Ya-Juan Li, Bing Yan,* and Ying Li[a]

Abstract: 1,3-Diphenyl-1,3-propanepione (DBM)-functionalized SBA-15 and SBA-16 mesoporous hybrid materials (DBM-SBA-15 and DBM-SBA-16) are synthesized by co-condensation of modified 1,3-diphenyl-1,3-propanepione (DBM-Si) and tetraethoxysilane (TEOS) in the presence of Pluronic P123 and Pluronic F127 as a template, respectively. The as-synthesized mesoporous hybrid material DBM-SBA-15 and DBM-SBA-16 are used as the first precursor, and the second precursor poly(methylacrylic acid) (PMAA) is synthesized through the addition polymerization reaction of the monomer methacrylic acid. These precursors then coordinate to lanthanide ions simultaneously, and the final mesoporous polymeric hybrid materials Ln(DBM-SBA-15)$_3$PMAA and Ln(DBM-SBA-16)$_3$PMAA (Ln = Eu, Tb) are obtained by a sol-gel process. For comparison, binary lanthanide SBA-15 and SBA-16 mesoporous hybrid materials (denoted as Ln(DBM-SBA-15)$_3$ and Ln(DBM-SBA-16)$_3$) are also synthesized. The luminescence properties of these resulting materials are characterized in detail, and the results reveal that ternary lanthanide mesoporous polymeric hybrid materials present stronger luminescence intensities, longer lifetimes, and higher luminescence quantum efficiencies than the binary lanthanide mesoporous hybrid materials. This indicates that the introduction of the organic polymer chain is a benefit for the luminescence properties of the overall hybrid system. In addition, the SBA-15 mesoporous hybrids show an overall increase in luminescence lifetime and quantum efficiency compared with SBA-16 mesoporous hybrids, indicating that SBA-15 is a better host material for the lanthanide complex than mesoporous silica SBA-16.

Keywords: lanthanides · luminescence · mesoporous materials · polymers · silicates

Introduction

Lanthanide complexes have long been the subject of extensive research owing to their excellent photophysical properties, which have a variety of potential technological applications, such as in fluoro-immunoassays, spectroscopic structural probes in biologically important systems, lasers, optical amplification, light-conversion molecular devices (LCMDs), and organic-light emitting diodes (OLEDs).[1] Considerable studies have been focused on the design and assembly of lanthanide complexes with organic ligands such as aromatic carboxylic acids, β-diketones, cryptands, calixarenes, and heterocyclic derivatives, which show strong absorption of ultraviolet light and then facilitate an effective intramolecular energy-transfer process to the central lanthanide ions (antenna effect).[2] As the absorption coefficients of organic ligands are many times larger than the molar absorption coefficients of trivalent lanthanide ions, the lanthanide complexes, especially those containing β-diketone ligands, exhibit the bright and narrow emission characteristic of metal ions, and offer several advantages and potential applications for the design of efficient light-conversion molecular devices.[3] However, they have so far been excluded from practical applications as tunable solid-state laser or phosphor devices largely owing to their poor stabilities under high temperature or moisture conditions and low mechanical strength. Recently, the luminescence properties of Re complexes supported on a solid matrix were studied extensively since their photophysical properties could be modified by interaction with the host structure.[4,5] Lanthanide complexes incorporated into inorganic or organic/inorganic matrix by a low-temperature soft-chemistry process, including the sol-gel

---

[a] Dr. Y.-J. Li, Prof. B. Yan, Dr. Y. Li
Department of Chemistry
Tong Ji University
Shanghai 200092 (China)
Fax: (+86) 21-65982287
E-mail: byan@tongji.edu.cn

Supporting information for this article is available on the WWW under http://dx.doi.org/10.1002/asia.201000032.

method and hydrothermal-synthesis process, can effectively overcome the disadvantages discussed above. The hybrid materials enable both inorganic and organic dopants to be incorporated with relatively high thermal stability.[6] However, the conventional doping method in a sol-gel procedure seems unable to solve the problems of clustering of emitting centers, inhomogeneous dispersion of the two phases, and leaching of the photoactive molecules, because only weak interactions (such as hydrogen bonding, van der Waals forces, and weak static effects) exist between the organic and inorganic components.[7] As a consequence, another appealing method has emerged that concerns the covalently bonded hybrids.The as-derived molecular-based materials exhibit improved chemical stability and have a monophasic appearance that is similar in nature to that of the complicated molecular polymeric Si–O network.[8] Our research group is concentrating on the design of the rare-earth hybrid materials with inorganic networks.[9] Compared with chemically bonded rare-earth hybrids with Si–O polymeric networks, fewer reports on molecular hybrid materials fabricated with rare-earth/organic polymers have been published,[10] which is possibly because suitable polymers or monomers are hard to select. Recently, more professional investigations have been altered to focus on the lanthanide hybrid materials concerning inorganic and organic polymerization reactions or imbedding certain polymers that contain long-carbon chains by covalent bonds. It has been proved that the hybrid materials with the inorganic networks and organic polymers with high molecular weight have many excellent properties such as strong luminescence and high stability.

Zeolites and mesoporous silica materials are attractive hosts for the preparation and investigation of inorganic–organic hybrid materials, presenting a successive ordering from the molecular up to the macroscopic scale.[11] Recently, Li and co-workers reported organolanthanide complexes assembled into zeolite L crystals, and the resulting materials exhibited excellent photoluminescence properties and good thermal stability.[11,12] Zeolite L can be synthesized in a size range starting from about 30 nm up to several thousand nm, whereas the other host mesoporous materials possess an adjustable pore size from 2 to 50 nm: currently, most work mainly concentrates on mesoporous materials as host for lanthanide complexes, which may be on account of the difficulties of the availability of zeolite crystals with a narrow particle-size distribution and well-defined morphology. Among mesoporous materials, SBA-15 has certainly become one of the most attractive hosts owing to its high hydrothermal stability and the presence of hexagonally ordered large mesopores (*p6mm* symmetry group) interconnected by complementary micropores. Recently, our group has reported the synthesis and luminescence properties of SBA-15 mesoporous materials covalently bonded with lanthanide complexes by the modified β-diketonates.[13] The results revealed that the obtained materials possessed good luminescence properties and photo- or thermal stabilities. Further to SBA-15, which is a channel-like ordered mesoporous material, mesoporous silica SBA-16 has also been considered as a good support on account of its 3D structure consisting of ordered interconnected spherical mesopores, which has a cubic cage-like structure with multidirectional and large-pore systems that allow good accessibility for both functionalization and adsorption.[14] However, to the best of our knowledge, the luminescence of a lanthanide complex supported on the functionalized SBA-16 has been rarely reported to date.[15] This is probably on account of the difficulties encountered in the synthesis and especially in the characterization of this material.

Abstract in Chinese:

本文通过介孔杂化材料（DBM-SBA-15/DBM-SBA-16）和聚合物（PMAA）同时和稀土离子发生配位反应从而制得了一类新型的有机无机介孔聚合物杂化材料$Ln(DBM-SBA-15)_3PMAA$和$Ln(DBM-SBA-16)_3PMAA$ (Ln = Eu, Tb)。首先，二苯甲酰甲烷（DBM）功能化的SBA-15和SBA-16型介孔杂化材料（DBM-SBA-15和DBM-SBA-16）是由改性的二苯甲酰甲烷（DBM-Si）与正硅酸乙酯(TEOS)分别在表面活性剂P123， F127做模板剂的条件下，通过水解共缩聚反应制得的。而第二配体聚甲基丙烯酸(PMAA)则是由单体甲基丙烯酸经过加聚反应而得到的。为了比较，我们也制备了相应的二元稀土介孔杂化材料$Ln(DBM-SBA-15)_3$和$Ln(DBM-SBA-16)_3$。荧光性质研究表明，与二元的稀土介孔杂化材料相比，三元的稀土介孔聚合物杂化材料显示出更强的相对荧光强度，更长的寿命以及更高的量子效率，从而表明聚合物的引入有利于改善整个杂化体系的发光性能。另外，SBA-15型的稀土介孔杂化材料在荧光寿命和量子效率上都明显高于SBA-16型稀土介孔杂化材料，表明相对于SBA-16来说，SBA-15是一种更好的镧系配合物的主体基质。

With the above considerations, we herein present the systematic and comparative study of the mesoporous materials covalently bonded with lanthanide complexes containing organic polymeric chains designated as $Ln(DBM\text{-}SBA\text{-}15)_3PMAA$ and $Ln(DBM\text{-}SBA\text{-}16)_3PMAA$ (Ln = Eu, Tb; DBM = 1,3-diphenyl-1,3-propanepione; DBM-SBA-15 and DBM-SBA-16 denote DBM-functionalized SBA-15 mesoporous material and DBM-functionalized SBA-16 material, respectively). For further comparison, SBA-15 and SBA-16 covalently bonded with the binary Ln^{3+} complex with DBM ligand were also synthesized and denoted as $Ln(DBM\text{-}SBA\text{-}15)_3$ and $Ln(DBM\text{-}SBA\text{-}16)_3$ (Ln = Eu, Tb), respectively. Full characterization and detailed studies of the luminescence properties of all synthesized materials were investigated and compared.

Results and Discussion

DBM-Functionalized Parent Materials (DBM-SBA-15 and DBM-SBA-16)

The presence of the organic ligand DBM covalently bonded to the mesoporous SBA-15 and SBA-16 were characterized by FTIR and UV absorption spectroscopy. Figure 1 depicts the FTIR spectra of DBM (A), DBM-Si (B), DBM-functionalized mesoporous material DBM-SBA-15 (C), and DBM-SBA-16 (D). Comparing the spectra of DBM (A) and DBM-Si (B), the vibration of $-CH_2-$ at 3059 cm^{-1} (A) was replaced by a strong broad band located at 2963 cm^{-1} (B), which originated from the three methylene groups of 3-(triethoxysilyl)-propyl isocyanate (TEPIC). Furthermore, the spectra of DBM-Si is dominated by ν (C–Si, 1164 cm^{-1}) and

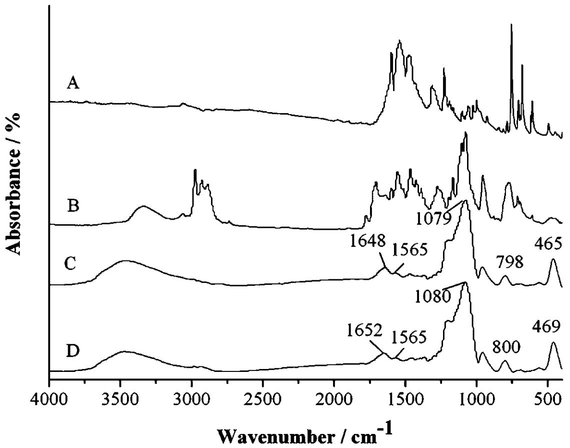

Figure 1. IR spectra of the free ligand DBM (A), the precursor DBM-Si (B), DBM-functionalized mesoporous material DBM-SBA-15 (C), and DBM-SBA-16 (D).

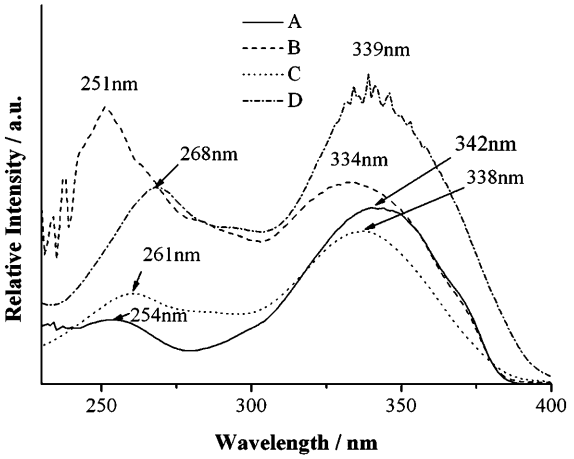

Figure 2. UV absorption spectra of A) DBM, B) DBM-Si, C) DBM-SBA-15, and D) DBM-SBA-16.

ν (Si−O, 1083 cm^{-1}) absorption bands, which is characteristic of trialkoxylsilyl functions. This evidence supports the emergence of DBM-Si. The band centered at 3335 cm^{-1} corresponds to the stretching vibration of grafted −NH− groups. Alternatively, the bending vibration (δ_{NH}, 1530 cm^{-1}) is further evidence of the formation of amide groups. New peaks at 1700 and 1630 cm^{-1} in (B) were attributed to the absorptions of the C=O of TEPIC, confirming that 3-(triethoxysilyl)-propyl isocyanate was successfully grafted onto the ligand DBM. In parts (C) and (D) of Figure 1, the formation of Si−O−Si is evidenced by the characteristic bands located at 1079, 1080 cm^{-1} (asymmetric vibrations ν_{as}, Si−O), 798, 800 cm^{-1} (stretching vibrations ν_s, Si−O), and 465, 469 cm^{-1} (in-plane bending vibrations δ, Si−O−Si). Bands at 1648, 1652, and 1565 cm^{-1}, originating from the −CONH− group of DBM-Si, can be observed in both DBM-functionalized mesoporous materials DBM-SBA-15 (C) and DBM-SBA-16 (D). This indicates that DBM-Si was successfully incorporated into both materials and preserved well after both hydrolysis/condensation reaction and surfactant extraction procedure, which is consistent with the fact that the DBM group in the framework remains intact after both hydrolysis–condensation reaction and the surfactant extraction procedure.

Figure 2 shows the ultraviolet absorption spectra of DBM (A), DBM-Si (B), DBM-SBA-15 (C), and DBM-SBA-16 (D). Comparing the absorption spectrum of DBM-Si (B) with that of DBM (A), we can see that an obvious blue shift of the major π–π* electronic transitions A→B (from 254 to 251 nm, from 342 to 334 nm) occurred, which indicates that the electron distribution of the modified DBM-Si has changed compared with the free ligand DBM owing to the introduction of carbonyl group and that the 3-(triethoxysilyl)-propyl isocyanate group has been successfully grafted to the ligand DBM. Compared with DBM-Si (B), the peak shape of DBM-SBA-15 (C) and DBM-SBA-16 (D) has basically not changed, but obvious red shifts (251→261, 334→338 nm for C, and 251→268, 334→339 nm for D) are observed, suggesting that more extensive π–π* conjugating systems were formed owing to the grafting reaction and the DBM groups were located on the surface of the mesoporous material SBA-15 and SBA-16.[13a]

Lanthanide (Eu^{3+}, Tb^{3+}) Complexes Covalently Bonded to DBM-Functionalized Mesoporous Silica and Polymers

Scheme 1 presents the scheme of the synthesis process and the predicted structure of the mesoporous hybrid materials Ln(DBM-SBA-16)$_3$PMAA. The modified ligands were covalently bonded to the SBA-16 host like an arm through Si−O−Si by the hydrolysis–condensation reaction of the organic functionality of DBM-Si. It is very difficult to prove the exact structure of this kind of non-crystalline hybrid materials and it is hardly possible to solve the coordination behavior of lanthanide ions. However, the main composition and co-ordination effect according to the lanthanide coordination chemistry principle and the configuration of the organic functional groups can be predicted. The rare earth positive ions are Lewis hard acids so it is easy to coordinate with the hard base containing the oxygen and nitrogen atoms. Additionally, most of the lanthanide complexes hold the polar covalent bonds as the lanthanide ions always bond through the 6s, 6p, and 5d electronic orbits, whose electron count is nine. Therefore, it is most stable for the lanthanide complex to exist with the coordination number of eight or nine. Furthermore, in our experiment we synthesize the material by adding the appropriate and accurate proportion of reagent into the system [Ln^{3+}:DBM-SBA-15 (DBM-SBA-16):PMAA = 1:3:2] to obtain the fixed model of lanthanide complex. Furthermore, in view of the spatial steric hindrance effect, we predicted the optimum coordination structure for the hybrid materials.

The FTIR spectra of all obtained mesoporous polymeric hybrids were measured and are shown in Figure S1 in the Supporting Information. The appearance of the −CONH− group at about 1557 and 1646 cm^{-1} for all samples demonstrates that the functionalized organic group DBM-Si re-

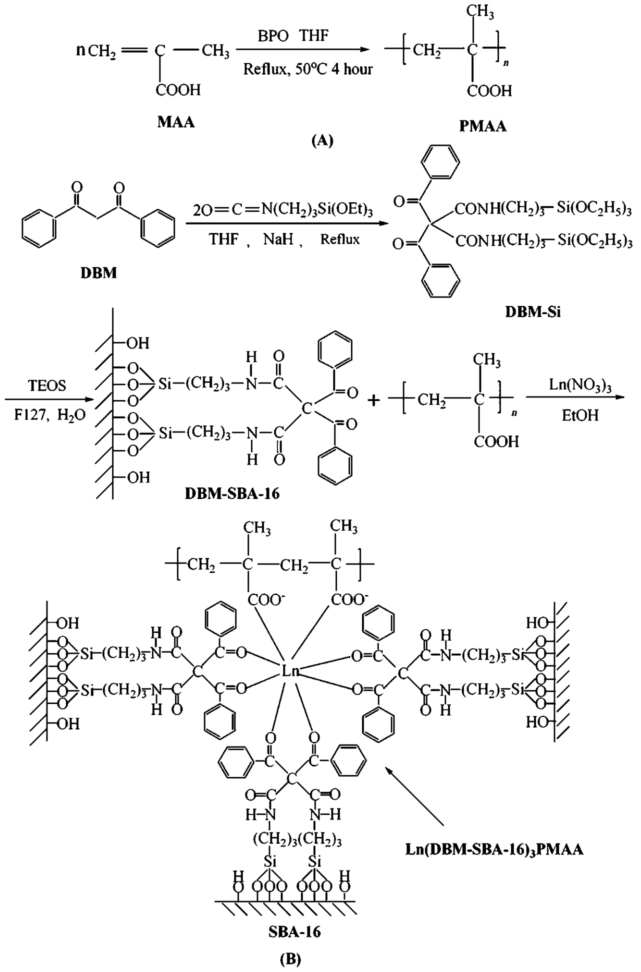

Scheme 1. A) Scheme showing the synthesis of the polymer precursor PMAA. B) The synthesis process of the mesoporous polymeric hybrids Ln(DBM-SBA-16)$_3$PMAA. BPO = benzoyl peroxide; TEOS = tetraethoxysilane.

mains intact after the hydrolysis/condensation reaction and complex-grafting process.[1c]

The powder XRD patterns of DBM-SBA-15 and DBM-SBA-16 before and after the introduction of Ln^{3+} complex (Ln = Eu, Tb) are shown in Figures 3 and 4, respectively. It can be observed that Ln(DBM-SBA-15)$_3$PMAA clearly show the order of the hexagonal array of the SBA-15 structure and exhibit a strong (100) reflection at a low angle and two small peaks (110, 200) at a higher angle. Although Ln(DBM-SBA-16)$_3$PMAA exhibits an intense (110) reflection and two small peaks owing to the (200) and (211) reflections, it can be indexed to the *Im*3*m* space group with cubic symmetry, which is typical of three-dimensional cubic (*Im*3*m*) SBA-16. Compared with those of DBM-SBA-15 and DBM-SBA-16 materials (see Table 1), the d_{100} spacing values of Ln(DBM-SBA-15)$_3$PMAA and Ln(DBM-SBA-16)$_3$PMAA are nearly unchanged, respectively, indicating that their framework ordering has been preserved well after the introduction of the lanthanide complex. It is also worth noting that the Ln(DBM-SBA-15)$_3$PMAA and Ln(DBM-

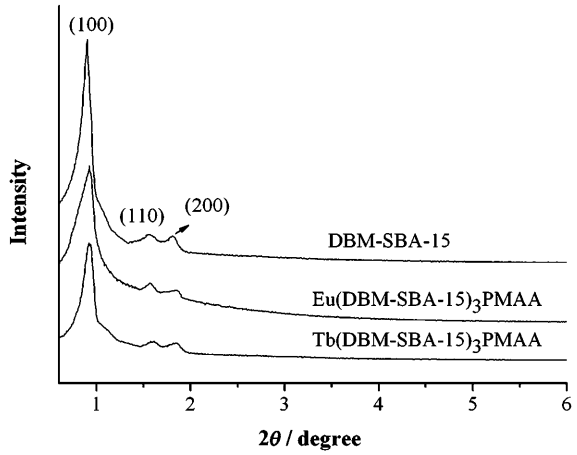

Figure 3. SAXRD patterns of DBM-SBA-15, Eu(DBM-SBA-15)$_3$PMAA, and Tb(DBM-SBA-15)$_3$PMAA.

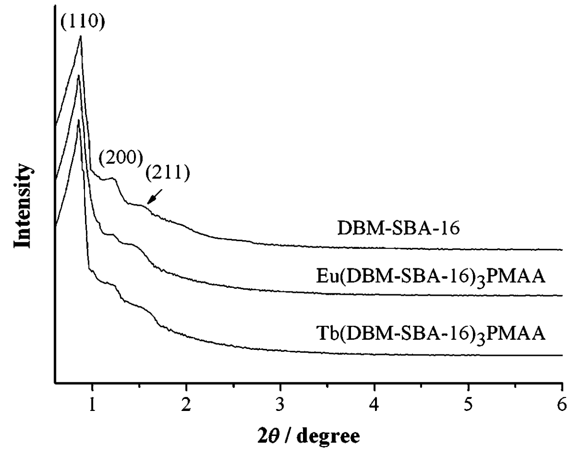

Figure 4. SAXRD patterns of DBM-SBA-16, Eu(DBM-SBA-16)$_3$PMAA, and Tb(DBM-SBA-16)$_3$PMAA.

Table 1. Structural parameters.

Sample	d[a] [nm]	a_0[b] [nm]	S_{BET}[c] [m^{2}g^{-1}]	V[c] [cm^{3}g^{-1}]	D_{BJH}[c] [nm]	t[d] [nm]
DBM-SBA-15	9.81	11.33	613	0.98	6.41	4.92
Eu(DBM-SBA-15)$_3$PMAA	9.63	11.12	569	0.59	4.16	6.96
Tb(DBM-SBA-15)$_3$PMAA	9.63	11.12	565	0.59	4.17	6.95
DBM-SBA-16	10.14	14.34	534	0.44	3.27	9.15
Eu(DBM-SBA-16)$_3$PMAA	10.38	14.68	433	0.29	2.63	10.08
Tb(DBM-SBA-16)$_3$PMAA	10.38	14.68	469	0.32	2.67	10.04

[a] The interplanar spacing for the most intense reflection peaks, (100) for the samples with *P6mm* symmetry group and (110) for the samples with *Im3m* symmetry group; [b] The unit cell parameter of SBA-15 was calculated by the formula $a_0 = 2\, d_{100}/\sqrt{3}$, and for SBA-16 by $\sqrt{2}\, d_{110}$; [c] S_{BET} = the BET surface area, V = the total pore volume, D_{BJH} = the average pore diameter; [d] The wall thickness, calculated by $a_0 - D_{BJH}$ for SBA-15 materials, and for SBA-15 materials by $\sqrt{3}a_0/2 - D_{BJH}$.

SBA-16)$_3$PMAA materials exhibit decreased diffraction intensity as compared to the parent DBM-SBA-15 and DBM-SBA-16 materials, respectively. This is probably owing to the presence of guest moieties on the mesoporous framework of SBA-15 and SBA-16, respectively, resulting in a decrease in the ordering degree but not the collapse of the pore structure of mesoporous materials.

The characterization of N_2 adsorption–desorption for Ln(DBM-SBA-15)$_3$PMAA and Ln(DBM-SBA-16)$_3$PMAA materials further provides proof of the preservation of the mesoporous structure after the introduction of the Ln^{3+} ion. As shown in Figure 5, Ln(DBM-SBA-15)$_3$PMAA exhibits typical type IV isotherms with distinct H1-type hysteresis loops at high relative pressures according to the IUPAC classification,[16] characteristic of mesoporous materials with highly uniform size distributions. Ln(DBM-SBA-16)$_3$PMAA shows the adsorption isotherms of the SBA-16 silica materials, which are of the type IV adsorption isotherm according to the IUPAC classification with H2-type hysteresis loops, which are typical for materials with ink-bottle pores with interconnectivity in a 3D pore system as a result of cavitation[17] (see Figure 6). The pore diameters (d), specific surface areas (S_{BET}), and pore volume (V) of these samples were calculated by the BJH method, and the results are summarized in Table 1. From d, S_{BET}, and V of DBM-SBA-15 and DBM-SBA-16, it can be seen that the data for both materials are less than those typically reported for pure SBA-15 and SBA-16 mesoporous silica materials, respectively.[47,48] This is probably as a result of the presence of organic ligand DBM on the pore surface and the co-surfactant effect of DBM-Si, which interacts with surfactant and reduces the diameter of the micelles. Furthermore, it can be observed that the values of S_{BET}, D, and V of the materials decreases after introducing the Ln^{3+} ion and organic ligand PMAA, which further confirmed incorporation of the Ln^{3+} complexes in the channels of SBA-15 and cavities of SBA-16.

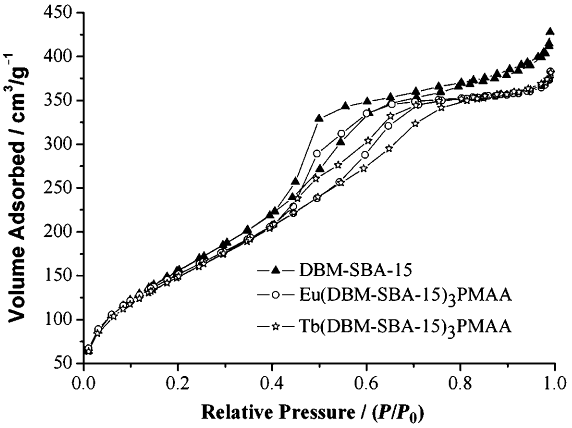

Figure 5. N_2 adsorption–desorption isotherms of DBM-SBA-15, Eu(DBM-SBA-15)$_3$PMAA, and Tb(DBM-SBA-15)$_3$PMAA.

The hexagonal mesostructures of Eu(DBM-SBA-15)$_3$PMAA and 3D mesostructured Eu(DBM-SBA-16)$_3$PMAA are further confirmed by TEM micrographs (see Figure 7). They present the regular hexagonal array of uniform channels and the well-ordered spherical cage structure, respectively, indicating that the mesostructure of the resulting materials can substantially be conserved after the complexation process, which concurs with the obtained XRD patterns. The distances between the centers of the mesopores for Eu(DBM-SBA-15)$_3$PMAA and Eu(DBM-SBA-16)$_3$PMAA are similar and estimated to be about 10 nm, which are in good agreement with the values determined from the corresponding XRD analysis (see Table 1).

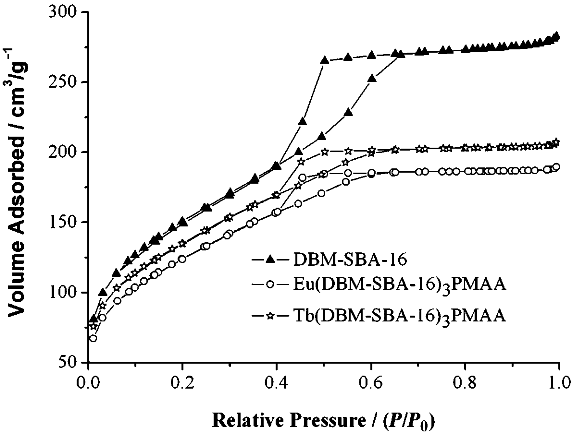

Figure 6. N_2 adsorption–desorption isotherms of DBM-SBA-16, Eu(DBM-SBA-16)$_3$PMAA, and Tb(DBM-SBA-16)$_3$PMAA.

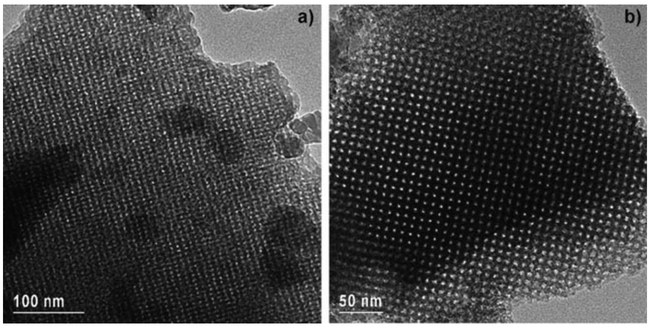

Figure 7. HRTEM images of Eu(DBM-SBA-15)$_3$PMAA (A) and Eu(DBM-SBA-16)$_3$PMAA (B).

Scanning Electron Micrographs

The scanning electron micrographs for the mesoporous polymeric hybrids demonstrate that homogeneous, molecular-based materials were obtained because of strong covalent bonds between the organic β-diketone ligand and the inorganic matrices, and the coordinate bonds between organic ligand β-diketone or polymer ligand and lanthanide ions, which belong to a complicated huge molecular system in nature. Compared with the hybrid materials with doped lanthanide complexes, which generally experience the phase-separation phenomena, herein we show that the inorganic and organic phases can exhibit their distinct properties together in the hybrid materials we obtained that contain covalent bonds.[18] Figure 8A and C show the regular gibbous particles on the surface, although the size of the particles is different, the former with the size of 3 μm and 10 μm for the latter. It is presumed that the time for sol-gel procedure of Eu(DBM-SBA-15)$_3$PMAA is longer than that of Eu(DBM-SBA-16)$_3$PMAA so that the longer process time avails the particle to grow in the three-dimensional directions. The microstructures of the material containing the Tb^{3+} ion display uniform stripes on the surface as can be seen in Figure 8B and D owing to the main influence derived from the Si–O networks as there is a trend to form the network-like microstructure in the sol-gel process.

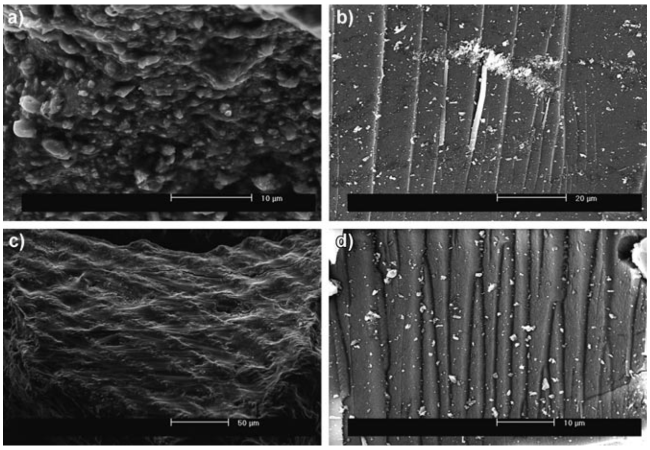

Figure 8. SEM images of the mesoporous polymeric hybrid materials Eu(DBM-SBA-15)$_3$PMAA (A), Tb(DBM-SBA-15)$_3$PMAA (B), Eu(DBM-SBA-16)$_3$PMAA (C), and Tb(DBM-SBA-16)$_3$PMAA (D).

Thermogravimetric Analysis

The thermal stability of all obtained mesoporous hybrids was demonstrated by TGA measurement. Figure 9 shows the thermogravimetric weight-loss curve (TGA) and derivative weight-loss (DrTGA) curve of mesoporous polymeric hybrid Eu(DBM-SBA-16)$_3$PMAA as an example. From the DrTGA curve, we can see that there are three main weight-loss peaks in the hybrid Eu(DBM-SBA-16)$_3$PMAA. The first weight-loss peak (approximately 5%) at around 100°C is owing to physically absorbed water. This is followed by a weight-loss peak (approximately 12%) at 300°C, which may be ascribed to the decomposition of incompletely removed surfactant.[19] The third weight-loss peak (approximately 14%) at 557°C can be attributed to the decomposition of the organic lanthanide complex. In addition, the weight-loss peak of the lanthanide hybrid material containing β-diketone and organic ligand PMAA was reported to be at about 406°C,[3c] suggesting that the thermal stability of the lanthanide complex was enhanced as it was covalently introduced into the mesoporous matrix.

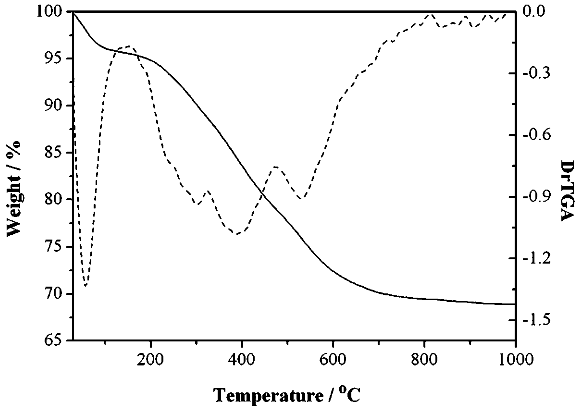

Figure 9. TGA (——) and DrTGA (– – –) curves of Tb(DBM-SBA-16)$_3$PMAA.

Photoluminescence Properties

The fluorescence excitation and emission spectra of the resulting europium and terbium mesoporous hybrids are shown in Figures 10 and 11, respectively. The excitation spectra were obtained by monitoring the emission of Eu^{3+} (Figure 10) or Tb^{3+} (Figure 11) ions at 613 or 545 nm and are dominated by a series of broad bands centered at about 331–356 or 328–332 nm near the ultraviolet region, respectively, which are attributed to the characteristic absorption of the lanthanide complexes arising from the efficient transition based on the conjugated C=O double bonds of 1,3-diphenyl-1,3-propanepione (DBM). As a result, Figure 10 provides the typical luminescence lines of the Eu^{3+} ion at about 577, 589, and 613 nm, corresponding to $^5D_0 \rightarrow ^7F_J$ transitions ($J = 0$, 1, and 2, respectively), and Figure 11 provides the

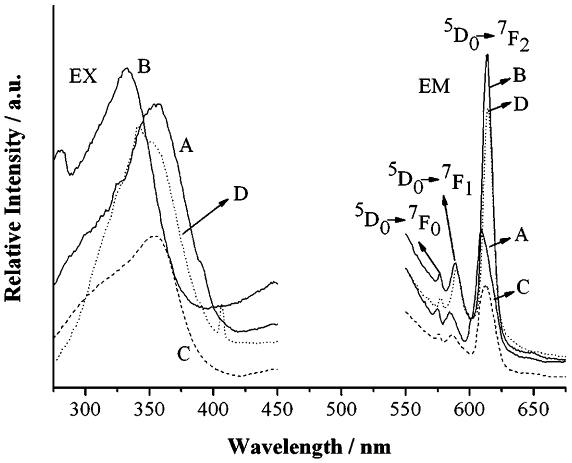

Figure 10. Luminescence excitation and emission spectra of the mesoporous hybrid materials: A) Eu(DBM-SBA-15)$_3$, B) Eu(DBM-SBA-15)$_3$PMAA , C) Eu(DBM-SBA-16)$_3$, and D) Eu(DBM-SBA-16)$_3$PMAA.

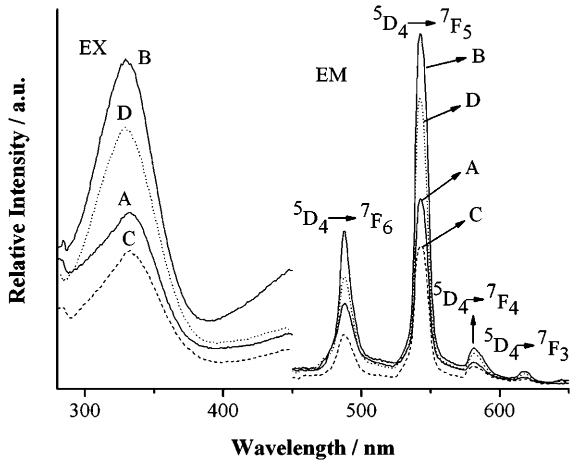

Figure 11. Luminescence excitation and emission spectra of the mesoporous hybrid materials: A) Tb(DBM-SBA-15)$_3$, B) Tb(DBM-SBA-15)$_3$PMAA C) Tb(DBM-SBA-16)$_3$, and D) Tb(DBM-SBA-16)$_3$PMAA.

typical luminescence lines of a Tb^{3+} ion at around 487, 542, 581, and 617 nm, which are assigned to the $^5D_4 \rightarrow {}^7F_J$ ($J=6$, 5, 4, and 3, respectively). Among these emission peaks, the prominent red luminescence ($^5D_4 \rightarrow {}^7F_5$) and green emissions ($^5D_0 \rightarrow {}^7F_2$) were observed in their emission spectra which indicated that the effective energy transfer took place between the modified organic ligand (DBM-Si) and the chelated lanthanide ions. The mesoporous hybrid materials show relatively strong emission owing to the chemically covalently bonded molecular Si−O network structure between the complex and the mesoporous silica. As seen from Figure 10, among the transitions of the materials containing Eu^{3+}, the $^5D_0 \rightarrow {}^7F_2$ at about 613 nm show the strongest emission. It is well-known that the $^5D_0 \rightarrow {}^7F_2$ transition is a typical electric dipole transition and strongly varies with the local symmetry of Eu^{3+}, whereas the $^5D_0 \rightarrow {}^7F_1$ transition corresponds to a parity-allowed magnetic dipole transition, which is independent of the host material. Therefore, the emission spectra indicate that the Eu^{3+} site is situated in an environment without inversion symmetry.[20]

In addition, the $^5D_0 \rightarrow {}^7F_1$ transition can be used as a reference to compare luminescence intensities of different Eu^{3+}-based materials owing to its magnetic dipole nature. The relative luminescence intensities of the $^5D_0 \rightarrow {}^7F_1$ transition (I_{01}) and the $^5D_0 \rightarrow {}^7F_2/{}^5D_0 \rightarrow {}^7F_1$ intensity ratios (red/orange ratio) for all materials are listed in Table 2. By comparison, it can be observed that the I_{01} value of the ternary complexes Eu(DBM-SBA-15)$_3$PMAA and Eu(DBM-SBA-16)$_3$PMAA are much higher than that of binary complex Eu(DBM-SBA-15)$_3$ and Eu(DBM-SBA-16)$_3$, respectively. There are two reasonable explanations that may contribute to the improved luminescence: one is that the oxygen atoms in carboxyl groups located in the polymer chains of PMAA coordinate to Ln^{3+} ions, which replace the coordinated water molecules that exist in complexes of aromatic carboxylic acid ligands, and the energy loss and clustering of the emitting centers caused by the vibration of the hydroxyl groups of coordinated water molecules is avoided. The other reason is that the more effective energy transfer took place from PMAA to the chelated Eu^{3+} ions and through this efficient method, leaching of the photoactive molecules can be avoided. Furthermore, a higher concentration of metal ions can be obtained and clustering of the emitting centers can be prevented because the hybrids belong to the molecular level. At the same time, it is also worth noting that compared with the SBA-16 mesoporous hybrids Eu(DBM-SBA-16)$_3$ and Eu(DBM-SBA-16)$_3$PMAA, the relative emission intensities and luminescence lifetimes of SBA-15 mesoporous hybrids Eu(DBM-SBA-15)$_3$ and Eu(DBM-SBA-15)$_3$PMAA exhibit obvious enhancements, which may be attributed to the fact that nonradiative (k_{nr}) transition probabilities are higher in SBA-16 mesoporous hybrids Eu(DBM-SBA-16)$_3$ and Eu(DBM-SBA-16)$_3$PMAA, despite the similar first coordination shells of the lanthanide ion to those of SBA-15 mesoporous hybrids Eu(DBM-SBA-15)$_3$ and Eu(DBM-SBA-15)$_3$PMAA, respectively. The fluorescence intensity and lifetimes of Tb^{3+} complexes shows the same rule. The detailed fluorescence data of Tb^{3+} complexes have been listed in Table 3.

Table 2. Photoluminescence data of europium hybrid mesoporous materials Eu(DBM-SBA-15)$_3$, Eu(DBM-SBA-15)$_3$PMAA, Eu(DBM-SBA-16)$_3$, and Eu(DBM-SBA-16)$_3$PMAA.

Hybrids	Eu(DBM-SBA-15)$_3$	Eu(DBM-SBA-15)$_3$PMAA	Eu(DBM-SBA-16)$_3$	Eu(DBM-SBA-15)$_3$PMAA
ν_{00}[a] [cm^{-1}]	17391	17331	17361	17301
ν_{01}[a] [cm^{-1}]	17123	16978	17036	16949
ν_{02}[a] [cm^{-1}]	16420	16287	16313	16287
I_{01}[b]	89.5	172	72.8	165
I_{02}[b]	218	459	142	384
I_{02}/I_{01}	2.09	2.67	1.95	2.33
τ[c] [ms]	0.265	0.448	0.206	0.369
τ_{exp}^{-1} [s^{-1}]	3774	2232	4854	2710
A_r [s^{-1}]	210	234	202	208
A_{nr} [s^{-1}]	3564	1998	4652	2502
η [%]	5.9	10.5	4.2	8.3

[a] The energies of the $^5D_0 \rightarrow {}^7F_J$ transitions (υ_{0J}); [b] The integrated intensity of the $^5D_0 \rightarrow {}^7F_J$ emission curves. [c] The luminescence decay times for $^5D_0 \rightarrow {}^7F_2$ transitions.

To further investigate the luminescence efficiency of these covalent hybrids, we measured the decay curves of the resulting europium and terbium mesoporous hybrid materials. The luminescence decay profiles relative to the eight materials could be fitted with single exponentials from which the room temperature fluorescence lifetimes were calculated to

Table 3. Photoluminescence data of terbium hybrid mesoporous materials $Tb(DBM\text{-}SBA\text{-}15)_3$, $Tb(DBM\text{-}SBA\text{-}15)_3PMAA$, $Tb(DBM\text{-}SBA\text{-}16)_3$, and $Tb(DBM\text{-}SBA\text{-}16)_3PMAA$.

Hybrids	Emission bands [nm]	Relative intensities[a]	Lifetime [ms][b]
$Tb(DBM\text{-}SBA\text{-}15)_3$	488, 542, 581, 617	180, 400, 56.6, 24.6	0.425
$Tb(DBM\text{-}SBA\text{-}15)_3PMAA$	487, 542, 581, 617	332, 748, 86.6, 36.6	0.553
$Tb(DBM\text{-}SBA\text{-}16)_3$	487, 543, 580, 617	115, 300, 48.2, 21.8	0.398
$Tb(DBM\text{-}SBA\text{-}16)_3PMAA$	488, 542, 581, 617	237, 612, 75.5, 32.5	0.479

[a] Relative intensities (arbitrary units) were obtained by the calculation of the integral area of the same emission bands; [b] For the $^5D_4 \rightarrow {}^7F_5$ transition of Tb^{3+}.

confirm that all the Ln^{3+} ions occupy the same average coordination environment. The resulting lifetimes of the Eu^{3+} and Tb^{3+} hybrids are given in Tables 2 and 3, respectively.

It was found that the rare-earth/inorganic/organic ternary polymeric hybrids $Ln(DBM\text{-}SBA\text{-}15)_3PMAA$ and $Ln(DBM\text{-}SBA\text{-}16)_3PMAA$ present longer luminescence lifetimes than the corresponding rare-earth/inorganic binary hybrids $Ln(DBM\text{-}SBA\text{-}15)_3$ and $Ln(DBM\text{-}SBA\text{-}16)_3$, which suggested that the introduction of organic polymeric chains can enhance the luminescence stability of the overall hybrid system. In addition, the DBM-SBA-15 mesoporous hybrids exhibit a longer lifetime than that of DBM-SBA-16 mesoporous hybrids, indicating that the nonradiative transition probability in DBM-SBA-16 mesoporous hybrids is higher than that in DBM-SBA-15 mesoporous hybrids. Furthermore, we selectively determined the emission quantum efficiencies (η) of the $^5D_0$ europium ion excited state for Eu^{3+} hybrids on the basis of the emission spectra and lifetimes of the $^5D_0$ emitting level. Assuming that only non-radiative and radiative processes are essentially involved in the depopulation of the $^5D_0$ state, radiative and nonradiative processes influence the experimental luminescence lifetime as can be seen in Equation (1).

$$\tau_{\exp} = (A_r + A_{nr})^{-1} \tag{1}$$

In Equation (1), A_r and A_{nr} are radiative and nonradiative transition rates, respectively. The quantum efficiency of the luminescence step, η, can be defined as how well the radiative processes compete with nonradiative processes as seen in Equation (2).[21]

$$\eta = A_r/(A_r + A_{nr}) \tag{2}$$

So, quantum efficiency can be calculated from the radiative transition rate constant and experimental luminescence lifetime from Equation (3).[22]

$$\eta = A_r \tau_{\exp} \tag{3}$$

A_r can also be obtained by summing over the radiative rates A_{0J} for each $^5D_0 \rightarrow {}^7F_J$ ($J=0$–4) transitions of Eu^{3+}, as in Equation (4).

$$A_r = \Sigma A_{0J} = A_{00} + A_{01} + A_{02} + A_{03} + A_{04} \tag{4}$$

The branching ratio for the $^5D_0 \rightarrow {}^7F_{5,6}$ transitions can be neglected as they are not detected experimentally and the influence of which can be ignored in the depopulation of the $^5D_0$ excited state. As $^5D_0 \rightarrow {}^7F_1$ belongs to the isolated magnetic dipole transition, it is practically independent of the chemical environments around the Eu^{3+} ion, and thus can be considered as an internal reference for the whole spectrum. The experimental coefficients of spontaneous emission, A_{0J} can be calculated according to Equation (5).[23]

$$A_{0J} = A_{01}(I_{0J}/I_{01})(\nu_{01}/\nu_{0J}) \tag{5}$$

In Equation (5), A_{0J} is the experimental coefficients of spontaneous emission and A_{01} is the Einstein coefficient of spontaneous emission between the $^5D_0$ and $^7F_1$ energy levels. In vacuum, A_{01} has a value of $14.65\ s^{-1}$, when an average index of refraction n equal to 1.506 was considered, the value of A_{01} can be determined to be approximately $50\ s^{-1}$ ($A_{01} = n^3 A_{01(vac)}$). I_{01} and I_{0J} are the integrated intensities of the $^5D_0 \rightarrow {}^7F_1$ and $^5D_0 \rightarrow {}^7F_J$ transitions ($J=0$–4) with ν_{01} and ν_{0J} ($\nu_{0J} = 1/\lambda_J$) energy centers, respectively. ν_{0J} refers to the energy barrier and can be determined from the emission bands of Eu^{3+}'s $^5D_0 \rightarrow {}^7F_J$ emission transitions. The emission intensity, I, taken as integrated intensity S of the $^5D_0 \rightarrow {}^7F_{0-4}$ emission curves, can be defined as shown in Equation (6).

$$I_{i-j} = \hbar\omega_{i-j} A_{i-j} N_i \approx S_{i-j} \tag{6}$$

In Equation (6), i and j are the initial ($^5D_0$) and final levels ($^7F_{0-4}$), respectively, ω_{i-j} is the transition energy, A_{i-j} is the Einstein coefficient of spontaneous emission, and N_i is the population of the $^5D_0$ emitting level.

On the basis of the above discussion, it can be seen the value h mainly depends on the values of two quanta: one is lifetime and the other is I_{02}/I_{01}. As can be clearly seen from Table 2, the quantum efficiency of the ternary mesoporous polymeric hybrid kinds $Eu(DBM\text{-}SBA\text{-}15)_3PMAA$ ($h = 10.5\%$) and $Eu(DBM\text{-}SBA\text{-}16)_3PMAA$ ($h = 8.31\%$) are much higher than the binary mesoporous hybrid $Eu(DBM\text{-}SBA\text{-}15)_3$ ($h = 5.9\%$) and $Eu(DBM\text{-}SBA\text{-}16)_3$ ($h = 4.2\%$), which can be explained as follows: each dispersed molecule is a luminescent unit so that the transparency, the dimension and concentration of dispersed lanthanide composite molecules and the interfacial interaction between the rare-earth organic complex and the polymer matrix are primary factors that influence the final luminescence properties of the materials. Compared with rare-earth hybrid materials synthesized through simple inorganic polymeric procedures, the larger interfacial region and the stronger interaction between the rare-earth complex and the polymer matrix in the obtained rare-earth/inorganic/organic polymeric hybrids might accelerate energy transfer between them and enhance the luminescence efficiency of the hybrids. In addition, compared with the SBA-16 mesoporous hybrids Eu(DBM-SBA-16)$_3$ and Eu(DBM-SBA-16)$_3$PMAA, the quantum efficiencies of SBA-15 mesoporous hybrids Eu(DBM-SBA-15)$_3$ and Eu(DBM-SBA-15)$_3$PMAA are higher, which may be ascribed to the following two aspects. One is that higher A_{nrad} parameter values occurred in SBA-16 mesoporous hybrids than in SBA-15 mesoporous hybrids; the other aspect is that the small pore diameters of SBA-16 mesoporous hybrids Eu(DBM-SBA-16)$_3$ and Eu(DBM-SBA-16)$_3$PMAA have an important effect on the results of the reflection and refraction of the Eu^{3+} ion luminescent center in the channel, which leads to the less-efficient intramolecular energy-transfer process (from ligand to Eu^{3+} ion).

Conclusions

In summary, we conducted a systematic and comparative study of the luminescent mesoporous polymeric hybrid materials Ln(DBM-SBA-15)$_3$PMAA and Ln(DBM-SBA-16)$_3$PMAA (Ln = Eu, Tb). They were prepared by linking ternary lanthanide (Eu^{3+}, Tb^{3+}) complexes to ordered mesoporous SBA-15 and SBA-16 through the functionalized DBM-Si ligand. Additionally, we prepared binary lanthanide complexes Ln(DBM-SBA-15)$_3$ and Ln(DBM-SBA-16)$_3$ for comparison. The structure and properties of all hybrid materials were characterized in detail. The results demonstrate that ternary rare-earth mesoporous polymeric hybrid materials present stronger luminescence intensities, longer lifetimes, and higher luminescence quantum efficiencies than the binary rare-earth mesoporous hybrid materials, which are attributed to the introduction of organic ligand PMAA. Furthermore, the SBA-15 mesoporous hybrids materials show an overall increase in luminescence intensity and lifetime compared with SBA-16 mesoporous hybrids, suggesting that the mesoporous material SBA-15 is a better candidate host for supporting the lanthanide complex than the mesoporous material SBA-16. However, the effect of the microenvironment between the organic complex and two kinds of silica matrix on the luminescence properties still needs further fundamental investigations.

Experimental Section

General

Ln(NO$_3$)$_3$ (Ln = Eu, Tb) were obtained by dissolving their respective oxides (Eu_2O_3 and Tb_4O_7) in concentrated nitric acid (HNO_3). Other chemicals were purchased and used as received. FTIR spectra were measured within the 4000–400 cm^{-1} region on an infrared spectrophotometer with the KBr pellet technique. The ultraviolet absorption spectra were taken with an Agilent 8453 spectrophotometer. X-ray powder diffraction patterns were recorded on a Rigaku D/max-rB diffractometer equipped with a Cu anode in a 2θ range from 0.6° to 6°. Nitrogen adsorption/desorption isotherms were measured at liquid-nitrogen temperature by using a Nova 1000 analyzer. Surface areas were calculated by the Brunauer-Emmett-Teller (BET) method and pore-size distributions were evaluated from the desorption branches of the nitrogen isotherms by using the Barrett-Joyner-Halenda (BJH) model. The fluorescence excitation and emission spectra were obtained on a Perkin–Elmer LS-55 spectrophotometer. Luminescence lifetime measurements were carried out on an Edinburgh FLS920 phosphorimeter by using a 450 W xenon lamp as excitation source. Scanning electron microscopy (SEM) was performed using the Philips XL30. Transmission electron microscopy (TEM) experiments were conducted on a JEOL2011 microscope operated at 200 kV or on a JEM-4000EX microscope operated at 400 kV. Thermogravimetric analysis (TGA) was performed on a Netzsch STA 409 at a heating rate of 15 °C min^{-1} under nitrogen atmosphere.

Syntheses

Polymer precursor (PMAA): Methacrylic acid (1 mmol, 0.087 g) was dissolved in a small quantity of the solution THF (6 mL) with the initiator benzoyl peroxide (BPO; 0.01 g) to initiate the addition polymerization under argon atmosphere purging. The reaction temperature was maintained at 50 °C for about 4 h. The coating liquid was concentrated at room temperature to remove the solvent THF by using a rotary vacuum evaporator, and the viscous liquid was obtained and identified as $[C_4H_6O_2]_n$ (see Figure 1 A). It was dissolved in DMF for the reaction with lanthanide ions.

DBM-functionalized SBA-15 mesoporous material (DBM-SBA-15): The modified precursor DBM-Si was synthesized according to the procedure reported in the literature: 1,3-diphenyl-1,3-propanepione (DBM; 1 mmol, 0.2243 g) was dissolved in 20 mL of dehydrated THF and then NaH (2 mmol, 0.048 g) was added into the solution with stirring. Two hours later, 3-(triethoxysilyl)-propyl-isocyanate (TEPIC; 2.2 mmol, 0.5442 g) was added dropwise into the refluxing solution. Then the mixture was heated at 65 °C in a covered flask for approximately 12 h under a nitrogen atmosphere. A yellow oil (the precursor DBM-Si) was furnished after isolation and purification. The mesoporous material DBM-SBA-15 was synthesized from acidic mixture with the following molar composition: 0.0172 P123:0.96 TEOS:0.04 DBM-Si:6 HCl:208.33 H_2O. P123 (1.0 g; TEOS = tetraethoxysilane) was firstly dissolved in the deionized water (7.5 g) and 2 M HCl solution (30 g) at 35 °C under vigorous stirring. A mixture of TEOS and DBM-Si (DBM = 1,3-diphenyl-1,3-propanepione) was added into the above solution, which was further stirred at 35 °C for 24 h and transferred into a Teflon bottle sealed in an autoclave. The autoclave was then heated at 100 °C for 24 h. The solid product was recovered by filtration, washed thoroughly with deionized water, and air dried at room temperature. Removal of copolymer surfactant P123 was conducted by Soxhlet extraction with ethanol for 48 h. The material was dried in a vacuum and showed a light-yellow color.

DBM-functionalized SBA-16 mesoporous material (DBM-SBA-16): The synthesis procedure of DBM-SBA-16 was similar to that of DBM-SBA-15 except that the copolymer surfactant P123 was replaced by F127, and the molar composition was 0.0040 F127:0.96 TEOS:0.04 DBM-Si:4 HCl:130 H_2O.

SBA-15 mesoporous material and polymer covalently bonded with ternary Ln^{3+} complexes (denoted as Ln(DBM-SBA-15)$_3$PMAA. Ln = Eu, Tb): The precursors DBM-SBA-15 and PMAA were dissolved in *N,N*-dimethyl formamide (DMF) solvent, and an appropriate amount of Ln(NO$_3$)$_3$ ethanol solution was added into the solution while stirring (the molar ratio of Ln^{3+}/DBM-SBA-15/PMAA = 1:3:1). The mixture was stirred at room temperature for 12 h, followed by filtration and extensive washing with EtOH. The resulting material Ln(DBM-SBA-15)$_3$PMAA was dried at 60 °C under vacuum overnight.

SBA-16 mesoporous material and polymer covalently bonded with ternary Ln^{3+} complexes (denoted as Ln(DBM-SBA-16)$_3$PMAA. Ln = Eu, Tb): The synthesis procedure of Ln(DBM-SBA-16)$_3$PMAA was similar to that of Ln(DBM-SBA-15)$_3$PMAA except that DBM-SBA-15 was replaced by DBM-SBA-16. The predicted structure of Ln(DBM-SBA-16)$_3$PMAA is shown in Scheme 1 B.

SBA-15 mesoporous material covalently bonded with the binary Ln^{3+} complexes (denoted as Ln(DBM-SBA-15)$_3$, Ln = Eu, Tb): The synthesis procedure for Ln(DBM-SBA-15)$_3$ was similar to that of Ln(DBM-SBA-

15)$_3$PMAA except that the mixed DMF solution of DBM-SBA-15 and PMAA was replaced by DBM-SBA-15.

SBA-16 mesoporous material covalently bonded with the binary Ln^{3+} complexes (denoted as Ln(DBM-SBA-16)$_3$, Ln = Eu, Tb): The synthesis procedure for Ln(DBM-SBA-16)$_3$ was similar to that of Ln(DBM-SBA-16)$_3$PMAA except that the mixed DMF solution of DBM-SBA-16 and PMAA was replaced by DBM-SBA-16.

Acknowledgements

This work was supported by the National Natural Science Foundation of China (20671072) and Program for New Century Excellent Talents in University (NCET-08-0398).

---

[1] a) C. Koeppen, S. Yamada, G. Jiang, A. F. Garito, L. R. Dalton, *J. Opt. Soc. Am. B* **1997**, *14*, 155–162; b) J. M. Lehn, *Angew. Chem.* **1990**, *102*, 1347–1362; *Angew. Chem. Int. Ed. Engl.* **1990**, *29*, 1304–1319; c) X. M. Guo, H. D. Guo, L. S. Fu, R. P. Deng, W. Chen, J. Feng, S. Dang, H. J. Zhang, *J. Phys. Chem. C* **2009**, *113*, 2603–2610; d) M. D. McGehee, T. B. Bergstedt, C. Zhang, A. P. Saab, M. B. O'Regan, G. C. Bazan, V. I. Srdanov, A. J. Heeger, *Adv. Mater.* **1999**, *11*, 1349–1354.

[2] a) C. J. Feng, Q. H. Luo, C. Y. Duan, *J. Chem. Soc. Dalton Trans.* **1998**, 1377–1380; b) T. Gunnlaugsson, A. J. Harte, J. P. Leonard, M. Nieuwenhuyzen, *Chem. Commun.* **2002**, 2134–2135; c) B. Yan, Y. S. Song, *J. Fluoresc.* **2004**, *14*, 289–294.

[3] a) F. S. Richardson, *Chem. Rev.* **1982**, *82*, 541–552; b) N. Sabbatini, M. Guardigli, J. M. Lehn, *Coord. Chem. Rev.* **1993**, *123*, 201–228; c) B. Yan, X. F. Qiao, *J. Phys. Chem. B* **2007**, *111*, 12362–12374.

[4] a) L. R. Matthews, E. T. Knobbe, *Chem. Mater.* **1993**, *5*, 1697–1700; b) P. A. Tanner, B. Yan, H. J. Zhang, *J. Mater. Sci.* **2000**, *35*, 4325–4328; c) C. Sanchez, B. Lebeau, F. Chaput, J. P. Boilot, *Adv. Mater.* **2003**, *15*, 1969–1994; d) S. M. Bruno, R. A. S. Ferreira, F. A. Almeida Paz, L. D. Carlos, M. Pillinger, P. Ribeiro-Claro, I. S. Gonçalves, *Inorg. Chem.* **2009**, *48*, 4882–4895.

[5] a) L. D. Carlos, R. A. S. Ferreira, V. D. Bermudez, S. J. L. Ribeiro, *Adv. Mater.* **2009**, *21*, 509–534; b) K. Binnemans, *Chem. Rev.* **2009**, *109*, 4283–4374.

[6] a) Q. M. Wang, B. Yan, *J. Mater. Chem.* **2004**, *14*, 2450–2454; b) B. Yan, Q. M. Wang, *J. Photochem. Photobiol. A* **2008**, *197*, 213–219.

[7] C. Sanchez, F. Ribot, *New J. Chem.* **1994**, *18*, 1007–1047.

[8] a) L. D. Carlos, R. A. S. Ferreira, J. P. Rainho, V. D. Bermudez, *Adv. Funct. Mater.* **2002**, *12*, 819–823; b) L. D. Carlos, R. A. Ferreira, R. N. Pereira, M. Assuncao and V. D. Bermudez, *J. Phys. Chem. B* **2004**, *108*, 14924–14932; c) K. Binnemans, P. Lenaerts, K. Driesen, C. Gorller-Walrand, *J. Mater. Chem.* **2004**, *14*, 191–195; d) S. S. Nobre, P. P. Lima, L. Mafra, R. A. S. Ferreira, R. O. Freire, L. S. Fu, U. Pischel, V. D. Bermudez, O. L. Malta, L. D. Carlos, *J. Phys. Chem. C* **2007**, *111*, 3275–3284; e) H. R. Li, J. Lin, H. J. Zhang and L. S. Fu, *Chem. Mater.* **2002**, *14*, 3651–3655.

[9] a) J. L. Liu, B. Yan, *J. Phys. Chem. B* **2008**, *112*, 10898–10907; b) H. F. Lu, B. Yan, J. L. Liu, *Inorg. Chem.* **2009**, *48*, 3966–3975; c) B. Yan, H. F. Lu, *Inorg. Chem.* **2008**, *47*, 5601–5611; d) B. Yan, Q. M. Wang, D. J. Ma, *Inorg. Chem.* **2009**, *48*, 36–44; e) J. L. Liu, B. Yan, *J. Phys. Chem. C* **2008**, *112*, 14168–14178.

[10] a) L. H. Wang, W. Wang, W. G. Zhang, E. T. Kang, W. Huang, *Chem. Mater.* **2000**, *12*, 2212–2218; b) H. Y. Chen, R. D. Archer, *Macromolecules* **1996**, *29*, 1957–1964; c) R. Iwamura, N. Higashiyama, K. Takemura, S. Tsutsumi, K. Kimura, G. Adachi, *Chem. Lett.* **1994**, 1131–1135; d) V. Bekiari, G. Pistolis, P. Lianos, *Chem. Mater.* **1999**, *11*, 3189–3195.

[11] Y. Wang, H. R. Li, Y. Feng, H. J. Zhang, G. Calzaferri, T. Z. Ren, *Angew. Chem.* **2010**, *122*, 1476–1480; *Angew. Chem. Int. Ed.* **2010**, *49*, 1434–1438.

[12] a) H. R. Li, W. J. Cheng, Y. Wang, B. Y. Liu, W. J. Zhang, H. J. Zhang, *Chem. Eur. J.* **2010**, *16*, 2125–2130; b) Y. G. Wang, H. R. Li, L. J. Gu, Q. Y. Gan, Y. N. Li, G. Calzaferri, *Microporous Mesoporous Mater.* **2009**, *121*, 1–6.

[13] a) Y. Li, B. Yan, H. Yang, *J. Phys. Chem. C* **2008**, *112*, 3959–3968; b) Y. J. Li, B. Yan, *Inorg. Chem.* **2009**, *48*, 8276–8285; c) Y. Li, B. Yan, *Dalton Trans.* **2010**, *39*, 1480–1487; d) L. L. Kong, B. Yan, Y. Li, *J. Solid State Chem.* **2009**, *182*, 1631–1637; e) Y. J. Li, B. Yan, Y. Li, *Microporous Mesoporous Mater.* **2010**, *131*, 82–88.

[14] D. Y. Zhao, Q. S. Huo, J. L. Feng, B. F. Chmelka, G. D. Stucky, *J. Am. Chem. Soc.* **1998**, *120*, 6024–6036.

[15] a) Y. J. Li, B. Yan, *Dalton Trans.* **2019**, *39*, 2554–2562; b) Y. J. Li, B. Yan, Y. Yi, *J. Solid State Chem.* **2010**, *183*, 871–877.

[16] a) K. S. W. Sing, D. H. Everett, R. A. W. Haul, L. Moscou, R. A. Pierotti, J. Rouquerol, T. Siemieniewska, *Pure Appl. Chem.* **1985**, *57*, 603–619; b) M. Kruk, M. Jaroniec, *Chem. Mater.* **2001**, *13*, 3169–3183.

[17] G. Chandrasekar, K. S. You, J. W. Ahn, W. S. Ahn, *Microporous Mesoporous Mater.* **2008**, *111*, 455–462.

[18] a) C. Y. Peng, H. J. Zhang, J. B. Yu, Q. G. Meng, L. S. Fu, H. R. Li, L. N. Sun, X. M. Guo, *J. Phys. Chem. B* **2005**, *109*, 15278–15287; b) W. J. Son, J. S. Choi, W. S. Ahn, *Microporous Mesoporous Mater.* **2008**, *113*, 31–40.

[19] R. A. Sá Ferreira, L. D. Carlos, R. R. Goncalves, S. J. L. Ribeiro, V. D. Bermudez, *Chem. Mater.* **2001**, *13*, 2991–2998.

[20] Q. Y. Hu, J. E. Hampsey, N. Jiang, C. J. Li, Y. F. Lu, *Chem. Mater.* **2005**, *17*, 1561–1569.

[21] a) Y. Hasegawa, M. Yamamuro, Y. Wada, N. Kanehisa, Y. Kai, S. Yanagida, *J. Phys. Chem. A* **2003**, *107*, 1697–1700; b) S. Surblé, C. Serre, F. Millange, F. Pelle, G. Ferey, *Solid State Sci.* **2007**, *9*, 131–136.

[22] a) M. H. V. Werts, R. T. F. Jukes, J. W. Verhoeven, *Phys. Chem. Chem. Phys.* **2002**, *4*, 1542–1548; b) E. E. S. Teotonio, J. G. P. Espinola, H. F. Brito, O. L. Malta, S. F. Oliveria, D. L. A. de Faria, C. M. S. Izumi, *Polyhedron* **2002**, *21*, 1837–1844; c) J. C. Boyer, F. Vetrone, J. A. Capobianco, A. Speghini, M. Bettinelli, *J. Phys. Chem. B* **2004**, *108*, 20137–20143.

[23] a) L. D. Carlos, Y. Messaddeq, H. F. Brito, R. A. Sá Ferreira, V. D. Bermudez and S. J. L. Ribeiro, *Adv. Mater.* **2000**, *12*, 594–598; Ferreira, V. D. Bermudez and S. J. L. Ribeiro, *Adv. Mater.* **2000**, *12*, 594–598; b) M. F. Hazenkamp, G. Blasse, *Chem. Mater.* **1990**, *2*, 105–110.

Received: January 13, 2010